Background Purification Framework With Extended Morphological Attribute Profile for Hyperspectral Anomaly Detection

Ju Huang ⓘ, Kang Liu ⓘ, Mingliang Xu ⓘ, Matjaž Perc ⓘ, and Xuelong Li ⓘ, *Fellow, IEEE*

Abstract—Hyperspectral anomaly detection has attracted extensive interests for its wide use in military and civilian fields, and three main categories of detection methods have been developed successively over past few decades, including statistical model-based, representation-based, and deep-learning-based methods. Most of these algorithms are essentially trying to construct proper background profiles, which describe the characteristics of background and then identify the pixels that do not conform to the profiles as anomalies. Apparently, the crucial issue is how to build an accurate background profile; however, the background profiles constructed by existing methods are not accurate enough. In this article, a novel and universal background purification framework with extended morphological attribute profiles is proposed. It explores the spatial characteristic of image and removes suspect anomaly pixels from the image to obtain a purified background. Moreover, three detectors with this framework covering different categories are also developed. The experiments implemented on four real hyperspectral images demonstrate that the background purification framework is effective, universal, and suitable. Furthermore, compared with other popular algorithms, the detectors with the framework perform well in terms of accuracy and efficiency.

Index Terms—Anomaly detection, background purification, extended attribute profile (EAP), hyperspectral image (HSI), sparse representation (SR), stacked autoencoder (SAE).

I. INTRODUCTION

HYPERSPECTRAL images (HSIs) involve hundreds of narrow bands in the spectral range from visible to infrared, which makes them provide nearly continuous spectral curves. Compared with other remote sensing images [1], HSIs can provide more abundant spectral information to recognize essential attributes of different land covers. Therefore, HSIs have shown advantages in various remote sensing applications, including scene classification [2], change detection [3], target detection [4], anomaly detection [5], etc. Among them, hyperspectral anomaly detection (HAD) has attracted much attention for its wide use in military and civilian fields [6]–[8]. HAD is a special target detection task, which is to detect rare and distinctive objects without any prior information about the target and the background [9].

In the past few decades, researchers have developed lots of methods based on different techniques. Generally speaking, most of the current HAD methods can be roughly divided into three categories: statistical-model-based, representation-based, and deep-learning-based. The statistical-model-based detectors were brought up early. The foremost work is the Reed–Xiaoli (RX) [10] detector. It assumes that the background data satisfy a multivariate Gaussian distribution, and anomaly pixels can be identified by computing the Mahalanobis distance between test pixel and statistical characteristics of the background. However, a multivariate Gaussian model is not exact enough for real HSIs; one major reason is that background modeling may be contaminated by anomaly pixels [11]. Some techniques are employed to improve the RX detector, including kernel technique [12], [13], Gaussian-mixture-model-based method [14], etc.

Another popular category is the representation-based methods. These methods are based on the assumption that background pixels can be approximately represented by a set of bases in a dictionary extracted from the original image, but anomalies cannot [15], [16]. The collaborative representation-based detector (CRD) [17] is another important work, which is based on the assumption that background pixels can be approximately constructed by their spatial neighbors. The low-rank decomposition technique [18] is introduced in the HAD task, which explores the low-rank properties of the background. Moreover, a tensor-decomposition-based method [19] is also researched.

The deep-learning-based methods have drawn much attention in HAD. Different from traditional algorithms, they can automatically learn the abstract and high-level feature representation. In [20] and [21], the autoencoder (AE), as a classical unsupervised feature learning model, is adopted to learn a hidden representation of input, and the reconstruction errors are used to identify anomalies. In addition, other networks, such

Ju Huang and Kang Liu are with the Shaanxi Key Laboratory of Ocean Optics, Xi'an Institute of Optics and Precision Mechanics, Chinese Academy of Sciences, Xi'an 710119, China, and also with the University of Chinese Academy of Sciences, Beijing 100049, China (e-mail: juhuang_iopen@163.com; liukang@opt.ac.cn).
Mingliang Xu is with the School of Information Engineering, Zhengzhou University, Zhengzhou 450001, China (e-mail: iexumingliang@zzu.edu.cn).
Matjaž Perc is with the Faculty of Natural Sciences and Mathematics, University of Maribor, 2000 Maribor, Slovenia (e-mail: matjaz.perc@gmail.com).
Xuelong Li is with the School of Artificial Intelligence, Optics and Electronics, Northwestern Polytechnical University, Xi'an 710072, China, and also with the Key Laboratory of Intelligent Interaction and Applications (Northwestern Polytechnical University), Ministry of Industry and Information Technology, Xi'an 710072, China (e-mail: li@nwpu.edu.cn).
Digital Object Identifier 10.1109/JSTARS.2021.3103858

as deep belief network [22], convolutional neural network [23], generative adversarial network [24], are utilized in HAD.

As a matter of fact, most of the aforementioned methods are essentially similar. They are all trying to construct the profile of the background [5] and then identify pixels that do not with meet the profile as anomalies. For the statistical-model-based methods, the profiles are the background statistical models. For the representation-based methods, the profiles are the background dictionaries, which are composed of a group of atoms extracted from the input image. For the deep-learning-based methods, the profiles are the learned network models. Due to the absence of prior information about anomaly and background, the whole image instead of the background is generally used to construct an approximate background profile. They are not accurate enough, although the proportion of anomalies is very low. Hence, it is necessary to filter the input in advance to obtain a purified background.

There are many ways to purify the background; some algorithms are based on the iterative strategy. For example, Taitano *et al.* [25] proposed a locally adaptable iterative RX method that purifies the background using the RX detector iteratively until the detection results being unchanged. In [26], the background dataset is expanded and updated by using the RX detector iteratively until the size of that being unchanged. Some methods are based on the probability statistics model. Gao *et al.* [27] proposed a probabilistic anomaly detector, which separates the HSI into anomalies and background with the RX detector via an automatic threshold. Additionally, some algorithms are based on suspected outlier removal. Zhang *et al.* [28] compared the similarity between each pixel and mean vector by using the spectral angle distance, and the pixels with larger distances are suspected outlier. In [29], Hou *et al.* proposed a collaboration representation with background purification and saliency weight (CRDBPSW) for HAD, where an outlier removal strategy based on representation coefficients is designed. However, the aforementioned methods, especially iterative-strategy-based, spend much computational time cost. Furthermore, they focus on the spectral difference between anomaly and background. Actually, anomaly objects have obvious difference in spatial domain, and they usually appear as isolated and small-size pixel blocks intuitively compared with the background. Hence, we can extract those pixel blocks and remove them to obtain a purified background. As we all know, the morphological attribute profiles (APs) [30] can extract different spatial characteristics of an image according to attribute settings; hence, we use this technique to obtain desired pixel blocks. As the AP is used to process a grayscale image, for a multivariate image (e.g., the HSI), the extended attribute profile (EAP) [31]–[33] is utilized instead. More specifically, we propose a novel background purification framework with extended morphological APs for HAD. This framework mainly consists of three key steps. First, the pixel blocks meeting with the given area attribute threshold are identified as suspected anomaly objects. Then, a strategy of background pixel selection is adopted according to the suspected anomaly detection map. Finally, the background dataset is used to obtain an accurate profile, and those pixels that do not meet with the profile are identified as anomalies.

To evaluate the effectiveness and applicability of our framework, we choose one classic and fundamental detector in each category and then employ the framework to improve it. The comparison experiments before and after using the framework will demonstrate its effectiveness. Compared with other popular methods, the detectors with this background purification framework all perform well in terms of efficiency and accuracy. To summarize, the major contributions are twofold.

1) Considering the difference between anomaly and background in spatial domain, a background purification framework with the extended morphological AP is presented, which can explore the spatial attributes of anomaly objects.
2) The framework can significantly improve the performance of existing three categories of HAD methods, merely adding a little more time. Furthermore, this framework is common, suitable, and parameter insensitive. We verify them on real datasets and obtain competitive results.

The rest of this article is organized as follows. Three typical and fundamental methods in each category are reviewed briefly in Section II. The proposed background purification framework and three anomaly detectors with this framework are detailedly introduced in Section III. Section IV shows the experiments and parameter analysis. Finally, Section V concludes this article.

II. RELATED WORKS

A. RX Detector

The RX detector is a classic statistical-model-based method. It is a constant false alarm rate (FAR) detector derived from the generalized likelihood ratio test [10]. The formula of the RX detector is as follows:

$$D_{\text{RX}} = (\mathbf{x} - \mu_0)^T \mathbf{\Sigma}^{-1} (\mathbf{x} - \mu_0) \qquad (1)$$

where D_{RX} is the detection result for a pixel vector $\mathbf{x}$, $\boldsymbol{\mu}_0$ is the background mean vector, and $\mathbf{\Sigma}$ is the background covariance matrix.

B. Sparse Representation (SR)-Based Detector

The SR-based detector is a fundamental representation-based method. The SR-based detectors assume that the background pixels can be constructed by a sparse linear combination of atoms in a background dictionary, whereas the anomaly pixels cannot. It can be described as follows:

$$\mathbf{x} = \mathbf{A}\alpha + \mathbf{N} \qquad (2)$$

where $\mathbf{A} \in \mathbb{R}^{p \times q}$ with $p \ll q$ is the background dictionary, N is the noise term, $\mathbf{x} \in \mathbb{R}^p$ is a pixel vector in the HSI, p is spectral dimension, and q is the number of atoms in $\mathbf{A}$.

We can obtain the sparse vector $\boldsymbol{\alpha}$ by solving the following optimization problem [15]:

$$\boldsymbol{\alpha} = \arg\min \|\mathbf{A}\boldsymbol{\alpha} - \mathbf{x}\|_2^2 \quad \text{s.t.} \ \|\boldsymbol{\alpha}\|_0 \leq K_0 \qquad (3)$$

where K_0 is the given upper bound on the sparsity level [34]. Obviously, the issue is NP-hard. Generally, there are two possible optimization methods: the greedy pursuit-based techniques [35],

[36] and the convex programming techniques [37]. Then, the reconstruction error is used to detect anomalies

$$r = \|\mathbf{x} - \mathbf{A}\hat{\alpha}\|_2^2 \tag{4}$$

where $\hat{\alpha}$ is an estimation of α and r is the reconstruction error; if r of a pixel $\mathbf{x}$ is larger than the given threshold, the pixel $\mathbf{x}$ is identified as anomaly.

C. Stacked Autoencoder (SAE)-Based Detector

The AE-based detector is a deep-learning-based method in HAD field. The AE learns a hidden representation and then recovers the original input from the hidden representation with an unsupervised manner [20], [38]. A single AE is composed of an encoder, a hidden layer, and a decoder. The training process of the AE contains two phases: encoder and decoder. Given a pixel $\mathbf{x} \in \mathbb{R}^p$, the input is mapped to a lower dimensional representation $\mathbf{y} \in \mathbb{R}^u$ by the encoder with the corresponding function:

$$\mathbf{y} = f\left(\mathbf{W}^{(1)}\mathbf{x} + \mathbf{b}^{(1)}\right) \tag{5}$$

where $u < p$. Then, the latent representation $\mathbf{y}$ is mapped back to an approximation $\tilde{\mathbf{x}}$ of the input $\mathbf{x}$ with the decoding function:

$$\tilde{\mathbf{x}} = g(\mathbf{W}^{(2)}\mathbf{y} + \mathbf{W}^{(2)}) \tag{6}$$

where $\tilde{\mathbf{x}} \in \mathbb{R}^p$ is the reconstruction of original input $\mathbf{x}$. $f(z) = g(z) = 1/(1 + \exp(-z))$ is the nonlinear activation function. $\boldsymbol{\theta} = (\mathbf{W}^{(1)}, \mathbf{b}^{(1)}, \mathbf{W}^{(2)}, \mathbf{b}^{(2)})$ are the network parameters. The training process of an AE is to find the optimal $\boldsymbol{\theta}$ to minimize the reconstruction error $J(\boldsymbol{\theta})$ [39]

$$J(\theta) = \frac{1}{2K} \sum_{i=1}^{K} (\|\mathbf{x}_i - \tilde{\mathbf{x}}_i\|_2^2) \tag{7}$$

where $\mathbf{x}_i, i = 1, 2, \ldots, K$, is the training pixels in HSI. The SAE consists of a multiple of single AEs. When the training process is ended, the reconstruction error can be used to detect anomalies. The average reconstruction error of training data is computed as

$$\varepsilon = \frac{1}{K} \sum_{i=1}^{K} (\|\mathbf{x}_i - \tilde{\mathbf{x}}_i\|_2^2). \tag{8}$$

A test pixel $\mathbf{x}$ is fed into the network to obtain the reconstruction $\tilde{\mathbf{x}}$ of the original input. Then, the reconstruction error r can be computed as follows:

$$r = \|\mathbf{x} - \tilde{\mathbf{x}}\|_2^2 > C\varepsilon \tag{9}$$

where C is the parameter according to the needs of users. The pixels whose reconstruction errors are greater than this threshold are identified as anomalies.

III. PROPOSED METHOD

Our background purification framework aims to acquire a pure background dataset, so as to make the background profile more accurate. In this section, the background purification framework is first introduced in detail. Based on this framework, three improved algorithms covering three main categories of existing

methods are then proposed. The flowchart of our framework is depicted in Fig. 1.

A. Suspected Anomaly Detection With EAPs

The AP [30] is based on the attribute filter. The attribute filter performs morphological transformation on the connected components (CCs) in a grayscale image, according to a criterion. More specifically, the criterion compares the attribute (e.g., area, diagonal length, volume, etc.) of a CC against a threshold κ. For example, if the attribute value of a CC is larger than κ, the CC will be unchanged; otherwise, it will be set as the gray value of their adjacent regions. If the gray value of the CC is brighten, the operation is called morphological attribute thickening; otherwise, it is called morphological attribute thinning. Attribute filters can be efficiently computed with the Max-tree algorithm [40]. It can be seen that the attribute filter can extract the CCs, whose attribute values are smaller than the predefined threshold κ; hence, we can use it to obtain desired pixel blocks. When the threshold is a sequence, the AP for a grayscale image is the combination of a group of attribute thickening and thinning operations [32].

Since the AP is for grayscale image, the multivariate image (e.g., HSI) should perform a feature reduction transformation [41], [42] first. The EAP for a multivariate image is assembled by the APs of its extracted features [31], [32]. Let an HSI be denoted as $\mathbf{I} \in \mathbb{R}^{w \times h \times p}$, where $w \times h$ is the spatial size and p is the number of the spectral bands. For convenience, the $\mathbf{I}$ is reshaped into a 2-D matrix $\mathbf{X} = \{x_i\}_{i=1}^n \in \mathbb{R}^{n \times p}$. First, the principal component analysis [41] is adopted to extract first d principal components (PCs). Then, the EAP for the HSI is computed as follows:

$$\mathbf{EAP} = \{\mathrm{AP}(\mathbf{PC}_1), \mathrm{AP}(\mathbf{PC}_2), \ldots, \mathrm{AP}(\mathbf{PC}_d)\}. \tag{10}$$

As for our framework, the main purpose is to find pixel blocks, whose attribute values are smaller than a predefined threshold, not to extract multilevel or multiattribute spatial features. Hence, we only select area attribute rather than multiple attributes, according to the spatial characteristic of anomaly objects. And we set the attribute threshold as a scalar κ rather than a sequence. The influence of parameter κ on detection performance is discussed in Section IV-D. The AP for each PC in this article is simplified as follows:

$$\mathrm{AP}(\mathbf{PC}_i) = \{\phi_\kappa^{\mathrm{aera}}(\mathbf{PC}_i), \mathbf{PC}_i, \gamma_\kappa^{\mathrm{aera}}(\mathbf{PC}_i)\}, \quad i = 1, \ldots, d \tag{11}$$

where $\phi_\kappa^{\mathrm{aera}}$ and $\gamma_\kappa^{\mathrm{aera}}$ denote morphological attribute thickening and thinning operators [43], respectively.

The morphological attribute thickening and thinning operations have already brighten and darken the desired pixel blocks. In order to extract and highlight the desired pixel blocks, a differential operation is adopted. Since $\phi_\kappa^{\mathrm{aera}}(\mathbf{PC}_i) > \mathbf{PC}_i$ and $\mathbf{PC}_i > \gamma_\kappa^{\mathrm{aera}}(\mathbf{PC}_i)$ are always satisfied according to the definition, the difference map for $\mathbf{PC}_i$ is computed as follows:

$$\mathbf{S}_i = |\phi_\kappa^{\mathrm{aera}}(\mathbf{PC}_i) - \mathbf{PC}_i| + |\mathbf{PC}_i - \gamma_\kappa^{\mathrm{aera}}(\mathbf{PC}_i)|$$
$$= \phi_\kappa^{\mathrm{aera}}(\mathbf{PC}_i) - \gamma_\kappa^{\mathrm{aera}}(\mathbf{PC}_i). \tag{12}$$
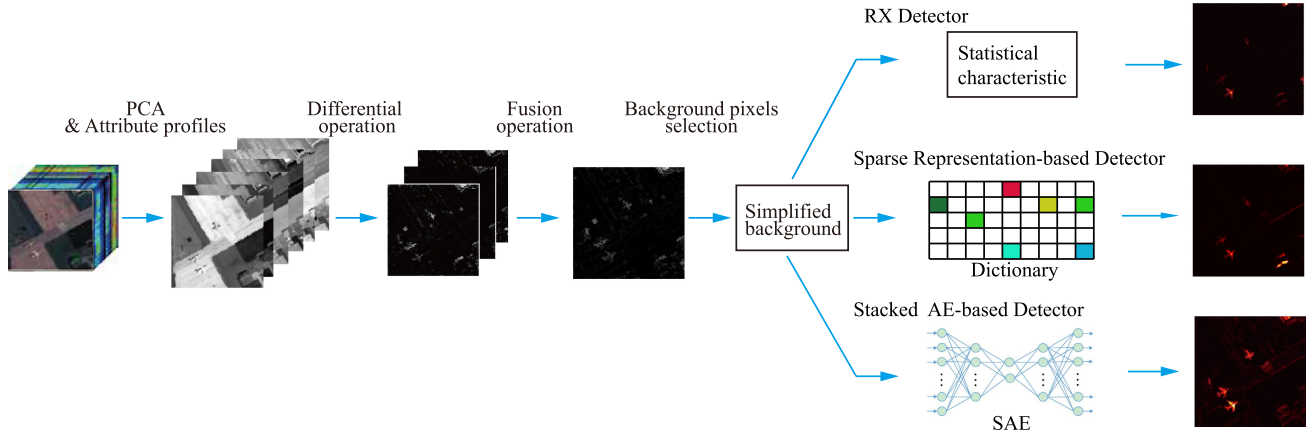
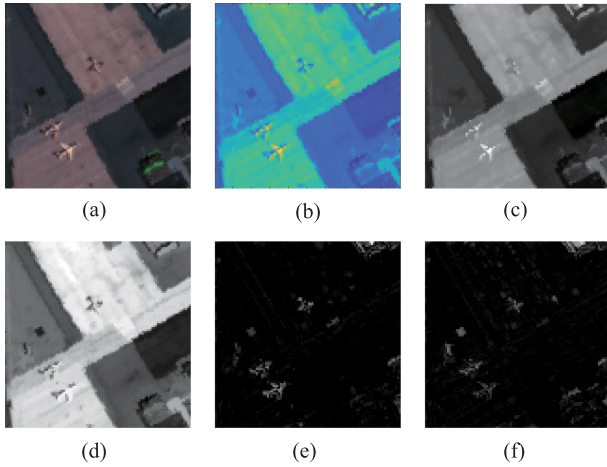Fig. 1.   Flowchart of the proposed method.

Fig. 2.   (a) Pseudocolor image of the San Diego dataset. (b) First PC of the image. (c) AP obtained by attribute thinning. (d) AP obtained by attribute thickening. (e) Difference map for the first PC. (f) Final suspected detection map.

Fig. 2(e) shows the difference map for $\mathbf{PC}_1$. Finally, the difference maps for all PCs are averaged to obtain the final suspected detection map, as shown in Fig. 2(f). The suspected anomaly detection map $\mathbf{D}$ is computed as follows:

$$\mathbf{D} = \frac{\sum_i^d \mathbf{S}_i}{d}. \tag{13}$$

B. Background Purification With Pixel Selection

In comparison with the background, anomaly objects generally appear as small and isolated pixel blocks from the perspective of spatial structure. Hence, with the help of the aforementioned step, the small-size pixel blocks can be detected, and those pixels can be roughly regarded as suspected anomalies. The AP, as a mathematical morphological methodology, only utilizes the spatial information of anomalies, so the detection results after the aforementioned step contain false anomaly targets. It is reasonable that removing those suspected anomalies from the original image can obtain the background dataset. Let the matrix $\mathbf{D}$ be sorted by value descending. Considering that the

proportion of anomaly pixels in an HSI is low generally, this framework selects the proportion η of the original image, whose position indices are corresponding to those of smaller values in matrix $\mathbf{D}$. The parameter η will be discussed in Section IV-D. Finally, the purified background $\mathbf{B}$ can be constructed with those selected pixels.

C. RX Detector With a Background Purification Framework

After the background purification step, the classic RX detector can be adopted to obtain the final detection map. The background mean vector and covariance matrix can be recalculated with the purified background $\mathbf{B}$

$$\tilde{\mathbf{\Sigma}} = \frac{1}{k} \sum_{i=1}^{\eta n} (\mathbf{x}_i - \mu_{\mathbf{B}}) (\mathbf{x}_i - \mu_{\mathbf{B}})^T \tag{14}$$

where $\tilde{\mathbf{\Sigma}}$ is the background covariance matrix and $\mu_{\mathbf{B}}$ is the background mean vector. The RX detector with a purified background can be computed as follows:

$$D_{\text{RX}}(\mathbf{x}_t) = (\mathbf{x}_t - \mu_{\mathbf{B}})^T \tilde{\mathbf{\Sigma}}^{-1} (\mathbf{x}_t - \mu_{\mathbf{B}}) \tag{15}$$

where $D_{\text{RX}}(\mathbf{x}_t)$ denotes the final detection result and $\mathbf{x}_t$ is the test pixel in the HSI. When the results of all pixel in $\mathbf{X}$ are computed, the final detection map is obtained. For convenience, this method is abbreviated as RX-BP in this article.

D. SR-Based Detector With a Background Purification Framework

After the background purification step, the next important work is to construct background dictionary $\mathbf{A}$ according to Section II-B. However, the dictionary $\mathbf{A}$ is unknown in advance and should contain as much background information as possible. One simple way is that the purified background $\mathbf{B}$ is used as dictionary. Obviously, it is impractical and time consuming. Another way is to randomly select some background pixels to form the dictionary $\mathbf{A}$. This way can reduce time cost, but may sacrifice some background information. As is conveyed by Fig. 4, the background scene is complex and covered by some kinds of major ground materials generally, and it is preferable
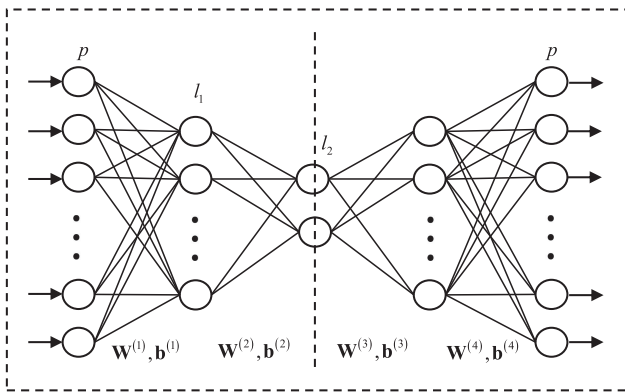
Fig. 3. SAE with three hidden layers. The output of the encoder is an abstract low-dimensional representation of the input. The output of the decoder is a reconstruction of the input.

that the dictionary $\mathbf{A}$ can cover all kinds of the ground materials. We can choose a small number of representative pixels in each class and assemble them to form the dictionary. Specifically, we use the K-means method to divide all pixels in $\mathbf{B}$ into K clusters and select some representative pixels in each cluster to form the dictionary. In addition, K is greater than the actual number of classes.

After the background $\mathbf{A}$ is obtained, the sparse $\boldsymbol{\alpha}$ is computed by solving (3). In our article, the problem in (3) is approximately solved by the orthogonal matching pursuit method [15]. Then, the residual error r of a test pixel $\mathbf{x}_t$ is computed as (4). When the reconstruction error r of each pixel is computed, the final detection map is obtained. For convenience, this method is abbreviated as SR-BP in this article.

E. SAE-Based Detector With a Background Framework

After the background purification step, the SAE network can be trained with the purified background. In this article, the architecture of the SAE stacked by two single AEs is shown in Fig. 3. The number of units in the input and output layers are equal to the number of spectral bands p. The number of units in the hidden layer is $\{l_1, l_2, l_3\}$, where $l_1 = l_3$. The $\mathbf{B}$ as the training dataset is used to update the network parameters $\theta = (\mathbf{W}^{(1)}, \mathbf{b}^{(1)}, \mathbf{W}^{(2)}, \mathbf{b}^{(2)}, \mathbf{W}^{(3)}, \mathbf{b}^{(3)}, \mathbf{W}^{(4)}, \mathbf{b}^{(4)})$ by minimizing the loss function as (7) with stochastic gradient descent.

When the SAE is trained, a test pixel $\mathbf{x}_t$ traverses through the network model to obtain the reconstruction $\tilde{\mathbf{x}}_t$. The reconstruction error r for $\mathbf{x}_t$ is computed as (9). When the reconstruction errors for each pixel are computed, the final detection map is obtained. For convenience, this method is abbreviated as SAE-BP in this article.

IV. EXPERIMENTS AND DISCUSSION

A. Datasets

Four different datasets covering various scenes are utilized to assess the performance of the proposed framework. These datasets have different properties, including satellite-borne data acquisition sensors, the diverse land covers, the size and type

of anomaly objects, etc. These datasets and the corresponding ground truths are download from a website.[1]

The first dataset is the San Diego dataset, which was collected by the airborne visible/infrared imaging spectrometer (AVIRIS) from the San Diego airport area, CA, USA. The size of the original image is 400×400, and a slice with the size of 100×100 is chosen as the test image. The spatial and spectral resolution is 3.5 m/pixel and 10 nm, respectively. This image has 189 spectral bands ranging from 370 to 2510 nm, after removing poor-quality bands. For this image, three airplanes are chosen as anomaly objects, and the background substances mainly include airstrips, hangars, and meadow. The pseudocolor image and the corresponding ground truth map are displayed in Fig. 4(a) and (e), respectively.

The second dataset is the HYDICE dataset, which was collected by the hyperspectral digital imagery collection experiment (HYDICE) sensor from an urban area, CA, USA. The size of original image is 307×307, and a slice with the size of 80×100 is selected as the test image. It has 175 spectral bands ranging from 400 to 2500 nm, after removing poor-quality bands. For this image, vehicles and buildings are taken as anomaly objects, and the background substances mainly include parking lots, pools, roads, and soil. The pseudocolor image and the corresponding ground truth map are displayed in Fig. 4(b) and (f), respectively.

The third dataset is the Urban dataset, which was also collected by the AVIRIS from an urban area, TX, USA. The size of selected test part is 100×100. The spectral resolution is 10 nm, and the spatial resolution is 17.2 m/pixel. This image has 204 spectral bands ranging from 400 to 1350 nm, after removing poor-quality bands. For this dataset, the houses are taken as anomaly objects, and the background substances mainly include meadow and vegetation. This image is heavily polluted by some strip noises, and it is a huge challenge to suppress the strip noises and recognize all anomalies simultaneously. The pseudocolor image and the corresponding ground truth map are shown in Fig. 4(c) and (g), respectively.

The fourth dataset is the Pavia dataset, which was captured by the reflective optics system imaging spectrometer over a city center in Pavia, Italy. The size of selected slice is 108×120. It has 102 spectral bands ranging from 430 to 860 nm, and its spatial resolution is 1.3 m/pixel. The background substances mainly include a bridge and water, and some vehicles in the bridge are taken as anomaly objects. The pseudocolor image and the corresponding ground truth map are shown in Fig. 4(d) and (h), respectively.

B. Comparison Methods and Evaluation Indexes

To evaluate the effectiveness of our proposed background purification framework, the comparison experiments between the original detector (i.e., RX [10], SR-based [15], and SAE-based [21]) and that with the background purification framework (i.e., RX-BP, SR-BP-based, and SAE-BP-based) will be carried out. The performance changes before and after using this framework will demonstrate the validity of the proposed

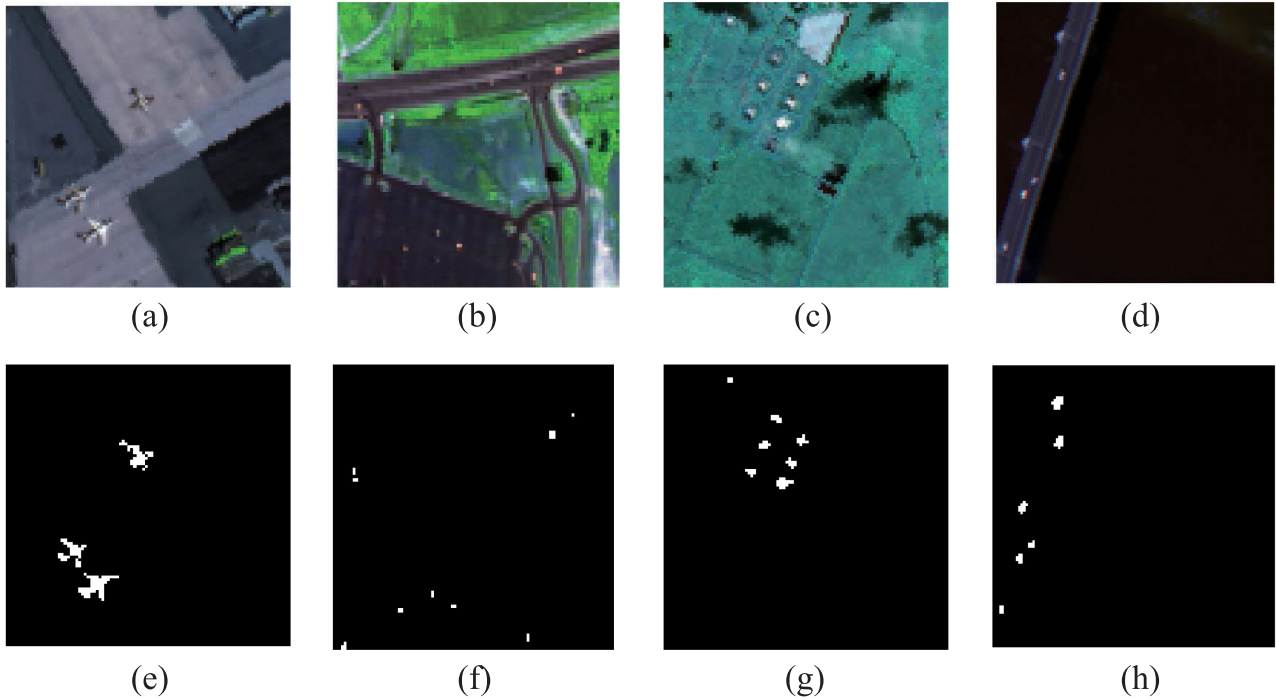[1][Online]. Available: http://xudongkang.weebly.com/

Fig. 4. San Diego dataset: (a) pseudocolor image and (e) ground truth. HYDICE dataset: (b) pseudocolor image and (f) ground truth. Urban dataset: (c) pseudocolor image and (g) ground truth. Pavia dataset: (d) pseudocolor image and (h) ground truth.

framework. Moreover, other popular algorithms are also selected as competitors, including CRD [17], CRDBPSW [29], BJSR [16], and kernel-isolation-forest-based detector (KIFD) [44]. Among them, the CRD and BJSR are classic representation-based methods, which employ collaborative representation and SR techniques, respectively. The CRDBPSW is based on background purification, which uses the representation coefficients to remove outlier automatically. The KIFD is a latest detection algorithm based on the theory of isolation forest, which split anomalies directly without constructing background profiles.

In order to assess and compare the performance of comparison methods, two evaluation indexes are utilized. One is the receiver operating characteristic (ROC) [45] curve, which describes the relationship between the detection probability (DP) and the FAR. The DP and the FAR are defined as

$$\text{DP} = \frac{P_D}{P_T}, \text{FAR} = \frac{P_F}{P} \qquad (16)$$

where P_D denotes the number of pixels, which are detected as anomalies. P_T denotes the total number of anomaly pixels, which are given in the ground truth, P_F denotes the number of pixels, which incorrectly detected as anomalies, and P denotes the total number of pixels in the image. If the curve of a detector is nearer to the top-left, it indicates that the detector has a better detection performance. The another is the area under ROC curve (AUC). If the AUC value of a detector is larger, it means the detector performs better.

Additionally, some critical parameters involved in the comparison experiments will be set in advance. For the background purification framework, the number of PCs d, the predefined area threshold κ, and the proportion η are set to 6, 25, and 85%, respectively. They are same on four datasets according to the parameter analysis in Section IV-D. For the specific three detectors, there are some extra parameters to set. Specifically, for the SR-based and SR-BP-based detectors, the parameter K is set as 25. For the SAE-based and SAE-BP-based detectors, the parameters $\{l_1, l_2, l_3\}$ are set to $\{48, 16, 48\}$, $\{32, 20, 32\}$, $\{48, 36, 48\}$, and $\{42, 36, 42\}$, respectively. These parameters are selected carefully according to the results of plenty of experiments. For other competitors, the optimal parameters are set according to the corresponding papers. The detection performance of the CRD, CRDBPSW, and BJSR is closely related to the window size (the inner window W_{in} and the outer window W_{out}). Hence, W_{in} is changed from 3 to 19, and W_{out} is changed from 7 to 35, in order to select the optimal window sizes. The regularization parameter λ for the CRD and CRDBPSW method is fixed at 10^{-6}. For the KIFD method, the parameters ζ, q, and M are set as 300, 1000, and $3\% \times N$ (N is the number of pixels in the HSI), respectively.

C. Detection Performance

For the San Diego dataset, the visualized results are shown in Fig. 5. In this picture, the results of comparison experiments before and after using this framework are marked with different color dotted boxes. It is obvious that the performance improvement is quite dramatic. For three classic methods, the framework can significantly suppress the influence of the background and reduce the FAR without sacrificing the DP. Moreover, compared with other competitors, the detectors with the framework, especially the SAE-BP-based detector, can not only locate anomaly objects but also recognize their shape information. The CRDBPSW method also does well on this dataset, but it is a little
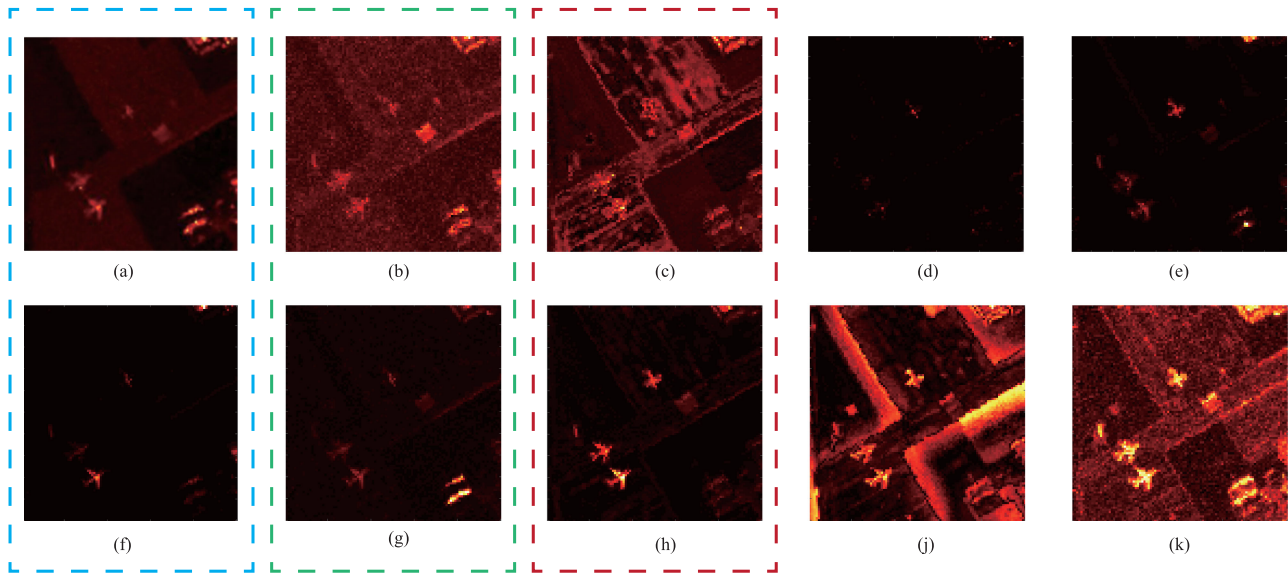
Fig. 5. Detection maps for the San Diego dataset. (a) RX detector. (b) SR-based detector. (c) SAE-based detector. (d) CRD. (e) CRDBPSW. (f) RX-BP-based detector. (g) SR-BP-based detector. (h) SAE-BP-based detector. (i) BJSR. (j) KIFD.
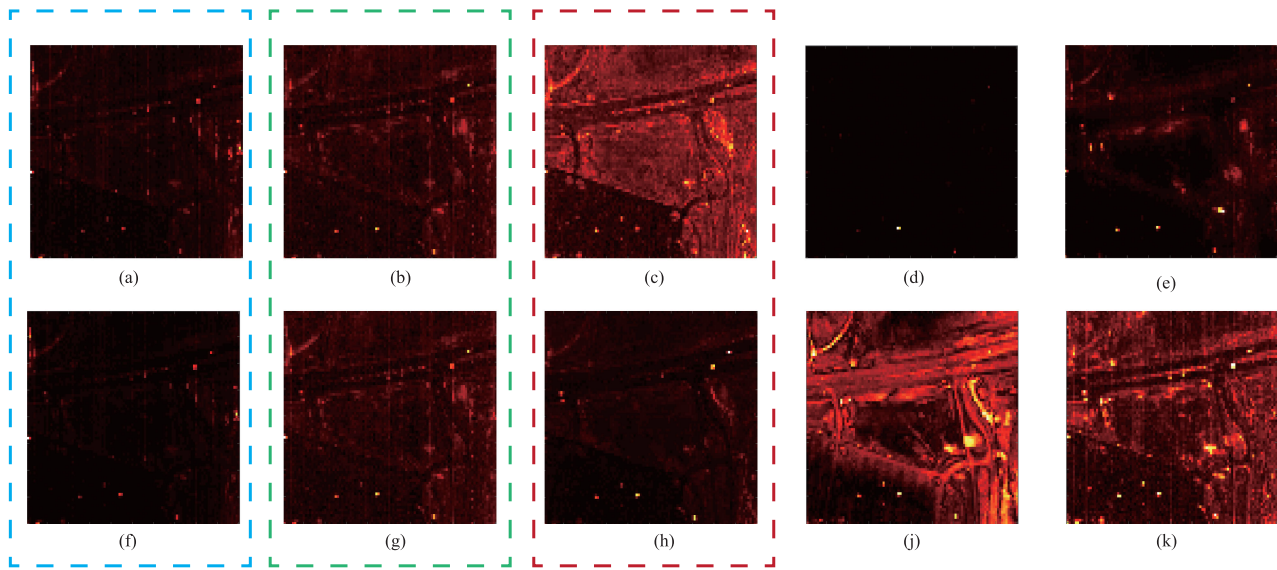

Fig. 6. Detection maps for the HYDICE dataset. (a) RX detector. (b) SR-based detector. (c) SAE-based detector. (d) CRD. (e) CRDBPSW. (f) RX-BP-based detector. (g) SR-BP-based detector. (h) SAE-BP-based detector. (i) BJSR. (j) KIFD.

worse than the SAE-BP-based detector. In order to illustrate the comparison results intuitively, the ROC curves are displayed in Fig. 7(a), and the AUC values are shown in the first column of Table I. It can be observed that the curves of the detectors with the background purification framework marked with thick lines are above on those without the proposed framework. The AUC values in Table I also prove the competitiveness; the AUC values of our proposed methods are 0.9784, 0.9665, and 0.9871, respectively.

For the HYDICE dataset, the visualized results are shown in Fig. 6. Similarly, the detection maps of comparison experiments before and after using our proposed framework are marked with different color dotted boxes. It can be observed that the

framework can reduce the FAR of the fundamental detector, especially for the SAE-based detector. In Fig. 6(h), the anomalies are detected, while background pixels are ignored, leading to high DP and low FAR. For the CRD detectors, few background pixels are falsely identified as anomalies, but few anomalies are correctly detected. The BJSR and KIFD methods have poor ability to separate the anomaly pixels and background pixels, leading to high FAR. Moreover, the ROC curves are displayed in Fig. 7(b), and the AUC values are shown in the second column of Table I. It can be observed that the curves of the detectors with the background purification framework marked with thick lines are nearer to the top-left than those without this framework, and the proposed RX-BP-Based detector has the best performance.
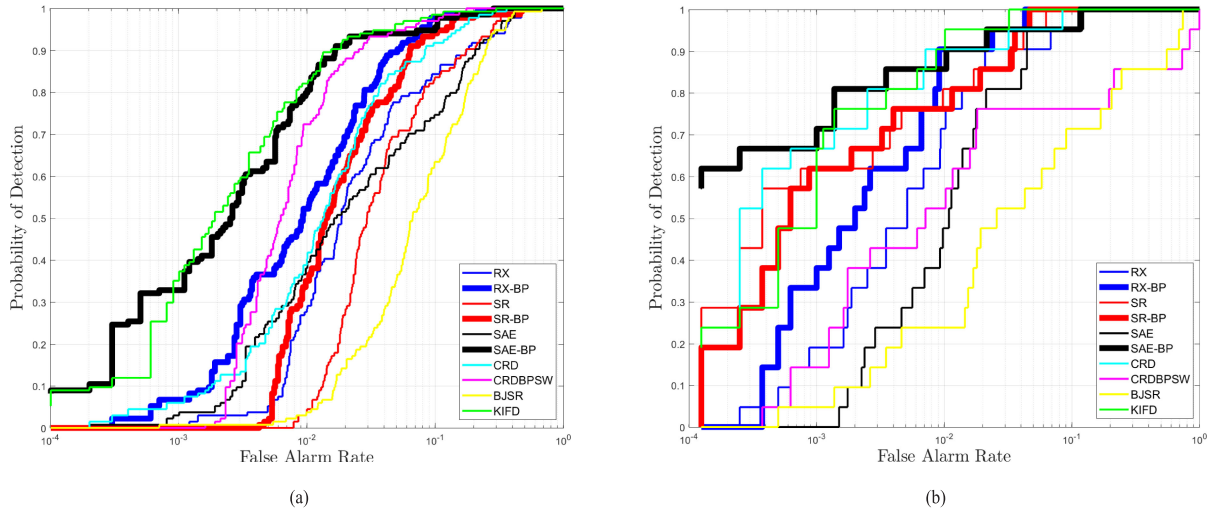
Fig. 7.   ROC curves of different algorithms on (a) the San Diego dataset and (b) the HYDICE dataset.

TABLE I
AUC VALUES OF COMPETITORS AND OUR PROPOSED DETECTORS
(I.E., RX-BP, SR-BP, AND SAE-BP) FOR FOUR DATASETS

	Data Sets			
Methods	San Diego	HYDICE	Urban	Pavia
RX	0.9403	0.9857	0.9907	0.9901
RX-BP	**0.9784**	**0.9940**	**0.9913**	**0.9982**
SR	0.9349	0.9914	0.9704	0.9660
SR-BP	**0.9665**	**0.9934**	**0.9966**	**0.9642**
SAE	0.9303	0.9807	0.9726	0.9832
SAE-BP	**0.9871**	**0.9926**	**0.9948**	**0.9942**
CRD	0.9678	0.9933	0.9669	0.9883
CRDBPSW	0.9864	0.9779	0.9755	0.9229
BJSR	0.8915	0.8573	0.9291	0.9558
KIFD	0.9906	0.9967	0.9374	0.7282

TABLE II
COMPUTING TIME (IN SECONDS) OF THE PROPOSED BACKGROUND
PURIFICATION FRAMEWORK FOR FOUR DATASETS

San Diego	HYDICE	Urban	Pavia
1.23	1.42	1.46	1.36

The AUC values also demonstrate the competitiveness, and the AUC values of the proposed three methods are 0.9940, 0.9934, and 0.9926, respectively.

For the Urban dataset, the visualized results are shown in Fig. 8. The detection maps of comparison experiments before and after using our proposed framework are marked with different color dotted boxes. It is clear that the effect of our background purification framework is quite dramatic. These detectors with our framework can suppress the strip noises to some extent. In particular, the RX-BP detector can detect all anomaly objects, while the nearly all of strip noises are well suppressed. Furthermore, the location and shape information of anomaly objects are very clear. The CRD and CRDBPSW methods can suppress strip noises effectively, but fail to identify some anomalies, leading to low DP. The SR-based, SAE-based, BJSR, and KIFD methods have poor ability to suppress the strip noise. Hence, it can be concluded that the statistical-model-based methods are better than the represented-based and deep-learning-based methods at wiping off strip noises. Moreover, the ROC curves and AUC values of competitors are shown in Fig. 10(a) and the third column of Table I, respectively. It can be seen that the curves of detectors with the background purification framework marked

with thick lines are closer to the top-left than those without the framework. Furthermore, the curves of the proposed detectors are above on those of competitors, and the curve of the SR-BP-based detector is closest to the top-left corner. The AUC values in Table I also prove the competitiveness; the AUC values of the proposed methods are 0.9913, 0.9966, and 0.9948, respectively.

For the Pavia dataset, the visualized results are shown in Fig. 9. The detection maps of comparison experiments before and after using our proposed framework are marked with different color dotted boxes. It can be observed that the framework can improve the detection performance. Compared with the SAE-based detector, the SAE-BP-based detector can avoid the edge of bridge being identified as anomalies. The BJSR, CRDBPSW, and KIFD methods perform poorly, and lots of background pixels, such as the edge of bridge, are falsely detected as anomalies. The CRD method has low FAR, but low DP. Moreover, the ROC curves are displayed in Fig. 10(b), and the AUC values are shown in the fourth column of Table I. We can find that the curves of detectors with the background purification framework marked with thick lines are nearer to the top-left corner than those without the framework. The AUC values in Table I also illustrate the superiority of our methods; the AUC values of our proposed methods are 0.9983, 0.9642, and 0.9942, respectively.

In addition, the time complexities are discussed. First, the computing time experiments of the background purification on four datasets are implemented, and the results are shown in Table II. Then, the computing time experiments of all competitors are carried out, and the results are shown in Table III. The SAE-based and SAE-BP-based detectors are performed using the software PyCharm 2020, and the others are performed
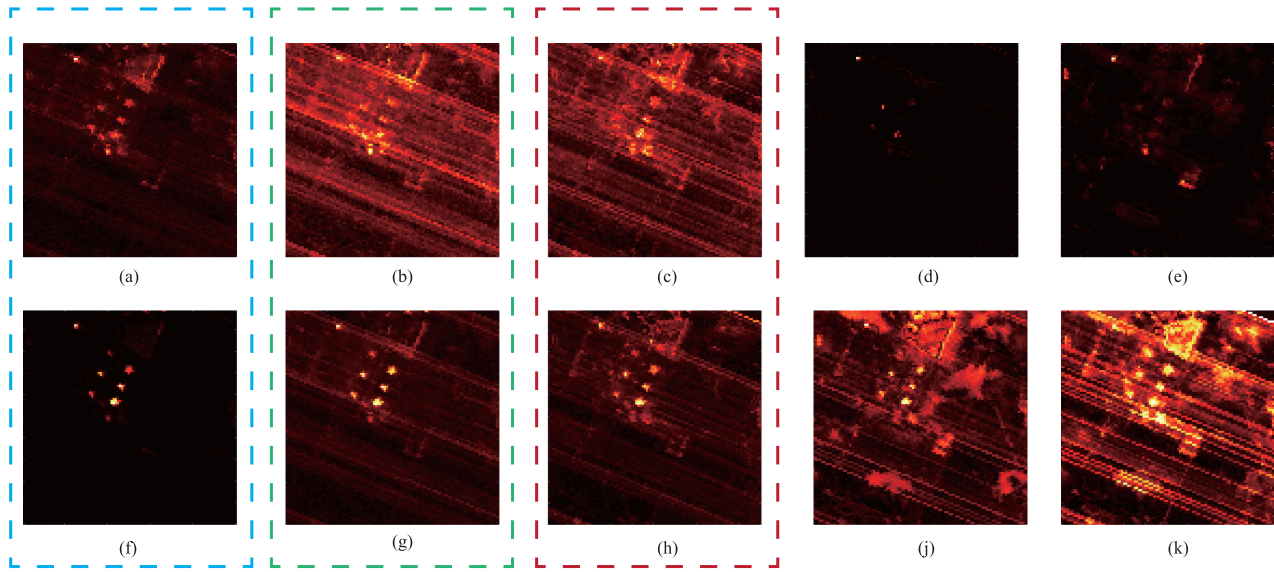
Fig. 8. Detection maps for the Urban dataset. (a) RX detector. (b) SR-based detector. (c) SAE-based detector. (d) CRD. (e) CRDBPSW. (f) RX-BP-based detector. (g) SR-BP-based detector. (h) SAE-BP-based detector. (i) BJSR. (j) KIFD.
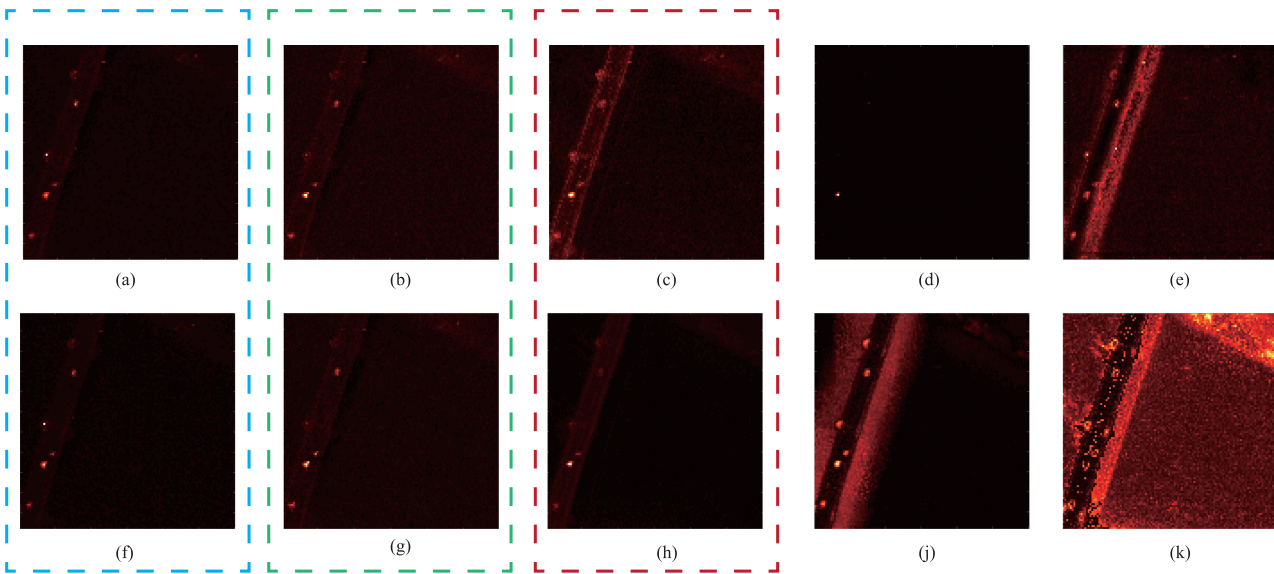

Fig. 9. Detection maps for the Pavia dataset. (a) RX detector. (b) SR-based detector. (c) SAE-based detector. (d) CRD. (e) CRDBPSW. (f) RX-BP-based detector. (g) SR-BP-based detector. (h) SAE-BP-based detector. (i) BJSR. (j) KIFD.

using the software MATLAB R2017a. The executing machine is a desktop with 2.9-GHz CPU and 16-GB RAM. The results demonstrate that the framework is highly efficient.

To summarize, the background purification framework can significantly improve the performance of RX, SR-based, and SAE-based detectors on four datasets, merely adding a little more time. The key point is that the framework can suppress the influence of the background and avoid the background pixels being identified as anomalies, yielding to low FAR. In addition, the selected detectors are representative and fundamental algorithms in each category of HAD methods. The selected datasets have different features, including the acquisition sensor,

spatial and spectral resolution, size of image, type and shape of anomaly objects, etc. It can be concluded that the background purification framework has extensive universality and suitability. Furthermore, compared with other competitors, the detectors with our framework all get good performance in terms of accuracy and efficiency.

D. Parameter Analysis and Discussion

The parameter analysis is performed on four real datasets. There are three parameters involved in the background purification framework: the number of PCs d, the predefined area
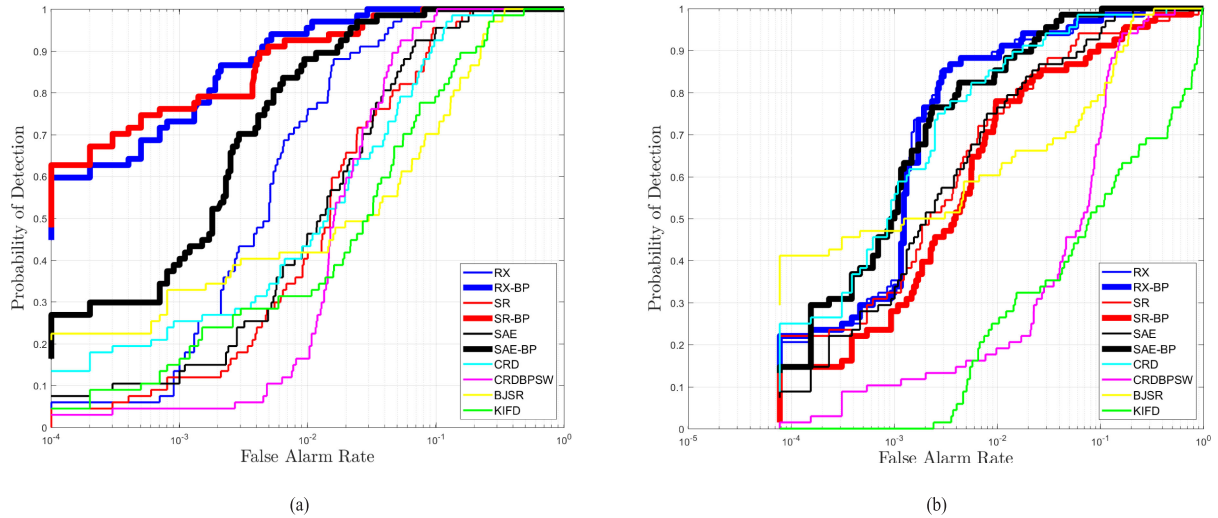
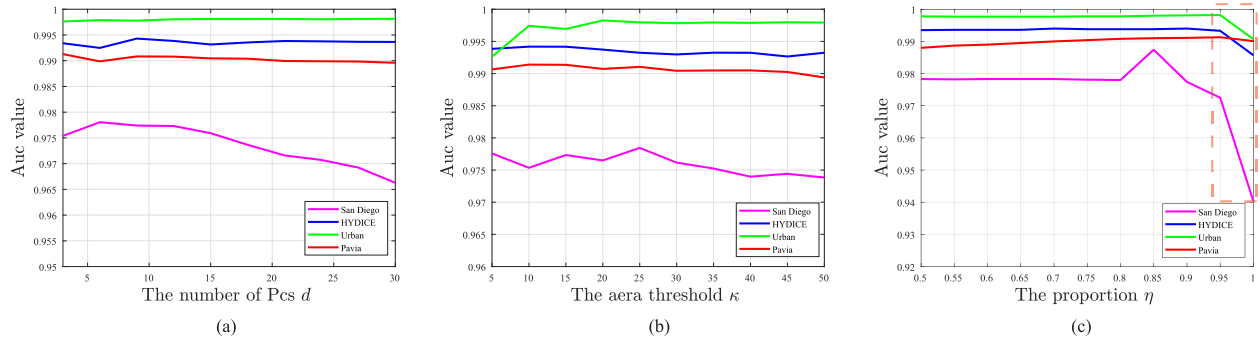Fig. 10.   ROC curves of different algorithms for (a) the Urban dataset and the (b) Pavia dataset.

Fig. 11.   Influence of the three parameters on detection performance of our proposed framework. (a) Number of PCs d. (b) Predefined area threshold κ. (c) Proportion η.

TABLE III
COMPUTING TIME (IN SECONDS) OF DIFFERENT METHODS FOR
FOUR DATASETS

Methods	Data Sets			
	San Diego	HYDICE	Urban	Pavia
RX	0.10	0.09	0.11	0.12
RX-BP	**1.34**	**1.52**	**1.57**	**1.49**
SR	135.74	77.62	118.40	98.28
SR-BP	**137.20**	**80.11**	**120.26**	**99.68**
SAE	53.44	48.30	52.63	58.12
SAE-BP	**55.88**	**50.32**	**54.18**	**60.68**
CRD	3553.78	2194.31	3830.12	2694.65
CRDBPSW	212.73	34.19	210.77	63.08
BJSR	5.33	3.88	6.25	5.94
KIFD	85.44	58.90	70.33	60.05

threshold κ, and the proportion η of overall pixels used to form the background dataset. Since the RX detector is nonparametric and concise, we take the RX-BP-based detector as the example to illustrate the influence of these three parameters on detection performance. Here, the AUC value is used to evaluate the detection performance.

1) Number of PCs d: The parameter d is the number of PCs, which determines the number of APs. Before performing this parameter experiment, the other two parameters κ and η are set as 20 and 0.85, respectively. The value of d varies from 3 to 30, and the AUC values on four datasets are shown in Fig. 11(a). It can be observed that the influences of d on performance are very small. For the San Diego dataset, the AUC values first increase, then reach the peak at 6, and finally decrease slowly.

2) Predefined Area Threshold κ: The parameter κ is the area threshold, which determines how big a pixel block needs to be removed. Similarly, the other two parameters d and η are set as 6 and 0.85, respectively, in advance. The value of κ varies from 5 to 50, and detection performance is shown in Fig. 11(b). It can be seen that the parameter κ has a little influence for the HYDICE and Pavia datasets. For the Urban dataset, the AUC value increases slightly as κ varies. For the San Diego dataset, the AUC value goes up and down irregularly.

3) Proportion η: The proportion η of overall pixels is selected to form the background $\mathbf{B}$. The larger the η is, the fewer suspect pixels are removed. The other two parameter d and κ are set as 6 and 20, respectively, in advance. The value of η varies from 0.5 to 1. $\eta = 1$ means none of pixels being removed. As shown

in Fig. 11(c), the area marked by the red dotted box illustrates that the proposed framework can significantly improve detection performance. For the HYDICE, Urban, and Pavia datasets, when η drops to 0.95, further reduction of η will not increase the AUC value. For the San Diego dataset, the turning point is at 0.85. The main reason is that the proportion of anomaly pixels in the HSI is very small. In reality, the proportion of anomaly pixels for four datasets is 1.34%, 0.26%, 0.67%, and 0.52%, respectively. We set the removal ratio to 5%.

As a whole, these three parameters discussed above have little influence on detection performance for the HYDICE, Urban, and Pavia datasets. However, these parameters have some effects for the San Diego dataset. The chief reasons are as follows: 1) the proportion of anomaly pixels in the San Diego dataset is larger than that in other three datasets; and 2) for the San Diego dataset, three airplanes are taken as anomaly objects by researchers; however, some other objects such as buildings can also be regarded as anomaly objects according to the definition of HAD, but they are not actually. In other words, anomalies are diverse. As for the other three datasets, the type and size of anomaly objects are similar.

V. CONCLUSION

In this article, we have developed a novel background purification framework with extended morphological APs for HAD. It can exploit the spatial property of anomalies to purify the background by removing suspected anomalies, in order to build an accurate background profile. Besides, three improved detectors belonging to different categories of HAD methods are also introduced with this framework. Since the selected datasets and methods are representative, the experiments with those can demonstrate that our background purification framework has effectiveness, universality, and applicability. In addition, three proposed detectors with the framework have good performance on four datasets.

REFERENCES

[1] Q. Tong, Y. Xue, and L. Zhang, "Progress in hyperspectral remote sensing science and technology in China over the past three decades," *IEEE J. Sel. Topics Appl. Earth Observ. Remote Sens.*, vol. 7, no. 1, pp. 70–91, Jan. 2014.

[2] Z. Meng, L. Jiao, M. Liang, and F. Zhao, "Hyperspectral image classification with mixed link networks," *IEEE J. Sel. Topics Appl. Earth Observ. Remote Sens.*, vol. 14, pp. 2494–2507, 2021.

[3] M. Hu, C. Wu, L. Zhang, and B. Du, "Hyperspectral anomaly change detection based on autoencoder," *IEEE J. Sel. Topics Appl. Earth Observ. Remote Sens.*, vol. 14, pp. 3750–3762, 2021.

[4] X. Zhao, W. Li, T. Shan, L. Li, and R. Tao, "Hyperspectral target detection by fractional Fourier transform," in *Proc. IEEE Int. Geosci. Remote Sens. Symp.*, 2020, pp. 1655–1658.

[5] Z. Wu, W. Zhu, J. Chanussot, Y. Xu, and S. Osher, "Hyperspectral anomaly detection via global and local joint modeling of background," *IEEE Trans. Signal Process.*, vol. 67, no. 14, pp. 3858–3869, Jul. 2019.

[6] M. Eismann, A. Stocker, and N. Nasrabadi, "Automated hyperspectral cueing for civilian search and rescue," *Proc. IEEE*, vol. 97, no. 6, pp. 1031–1055, Jun. 2009.

[7] Z. Gao, Y. Shao, G. Xuan, Y. Wang, Y. Liu, and X. Han, "Real-time hyperspectral imaging for the in-field estimation of strawberry ripeness with deep learning," *Aritif. Intell. Agriculture*, vol. 4, no. 1, pp. 31–38, 2020.

[8] F. Kruse, J. Boardman, and J. Huntington, "Comparison of airborne hyperspectral data and EO-1 Hyperion for mineral mapping," *IEEE Trans. Geosci. Remote Sens.*, vol. 41, no. 6, pp. 1388–1400, Jun. 2003.

[9] S. Matteoli, M. Diani, and G. Corsini, "A tutorial overview of anomaly detection in hyperspectral images," *IEEE Aerosp. Electron. Syst. Mag.*, vol. 25, no. 7, pp. 5–28, Jul. 2010.

[10] I. Reed and X. Yu, "Adaptive multiple-band CFAR detection of an optical pattern with unknown spectral distribution," *IEEE Trans. Acoust., Speech, Signal Process.*, vol. 38, no. 10, pp. 1760–1770, Oct. 1990.

[11] S. Matteoli, M. Diani, and J. Theiler, "An overview of background modeling for detection of targets and anomalies in hyperspectral remotely sensed imagery," *IEEE J. Sel. Topics Appl. Earth Observ. Remote Sens.*, vol. 7, no. 6, pp. 2317–2336, Jun. 2014.

[12] H. Kwon and N. Nasrabadi, "Kernel RX-algorithm: A nonlinear anomaly detector for hyperspectral imagery," *IEEE Trans. Geosci. Remote Sens.*, vol. 43, no. 2, pp. 388–397, Feb. 2005.

[13] J. Zhou, C. Kwan, B. Ayhan, and M. T. Eismann, "A novel cluster Kernel RX algorithm for anomaly and change detection using hyperspectral images," *IEEE Trans. Geosci. Remote Sens.*, vol. 54, no. 11, pp. 6497–6504, Nov. 2016.

[14] M. Carlotto, "A cluster-based approach for detecting man-made objects and changes in imagery," *IEEE Trans. Geosci. Remote Sens.*, vol. 43, no. 2, pp. 374–387, Feb. 2005.

[15] Y. Chen, N. Nasrabadi, and T. Tran, "Sparse representation for target detection in hyperspectral imagery," *IEEE J. Sel. Topics Signal Process.*, vol. 5, no. 3, pp. 629–640, Jun. 2011.

[16] J. Li, H. Zhang, L. Zhang, and L. Ma, "Hyperspectral anomaly detection by the use of background joint sparse representation," *IEEE J. Sel. Topics Appl. Earth Observ. Remote Sens.*, vol. 8, no. 6, pp. 2523–2533, Jun. 2015.

[17] W. Li and Q. Du, "Collaborative representation for hyperspectral anomaly detection," *IEEE Trans. Geosci. Remote Sens.*, vol. 53, no. 3, pp. 1463–1474, Mar. 2015.

[18] Y. Xu, Z. Wu, J. Li, A. Plaza, and Z. Wei, "Anomaly detection in hyperspectral images based on low-rank and sparse representation," *IEEE Trans. Geosci. Remote Sens.*, vol. 54, no. 4, pp. 1990–2000, Apr. 2016.

[19] Y. Xu, Z. Wu, J. Chanussot, and Z. Wei, "Joint reconstruction and anomaly detection from compressive hyperspectral images using Mahalanobis distance-regularized tensor RPCA," *IEEE Trans. Geosci. Remote Sens.*, vol. 56, no. 5, pp. 2919–2930, May 2018.

[20] E. Bati, A. Çalişkan, A. Koz, and A. Alatan, "Hyperspectral anomaly detection method based on auto-encoder," *Proc. SPIE*, vol. 9643, pp. 220–226, 2015.

[21] C. Zhao, X. Li, and H. Zhu, "Hyperspectral anomaly detection based on stacked denoising autoencoders," *J. Appl. Remote Sens.*, vol. 11, no. 4, 2017, Art. no. 042605.

[22] N. Ma, Y. Peng, S. Wang, and P. Leong, "An unsupervised deep hyperspectral anomaly detector," *Sensors*, vol. 18, no. 3, 2018, Art. no. 693.

[23] W. Li, G. Wu, and Q. Du, "Transferred deep learning for anomaly detection in hyperspectral imagery," *IEEE Geosci. Remote Sens. Lett.*, vol. 14, no. 5, pp. 597–601, May 2017.

[24] S. Arisoy, N. Nasrabadi, and K. Kayabol, "GAN-based hyperspectral anomaly detection," in *Proc. 28th Eur. Signal Process. Conf.*, 2021, pp. 1891–1895.

[25] Y. Taitano, B. Geier, and K. Bauer, "A locally adaptable iterative RX detector," *EURASIP J. Adv. Signal Process.*, vol. 2010, 2010, Art. no. 341908.

[26] N. Billor, A. Hadi, and P. Velleman, "BACON: Blocked adaptive computationally efficient outlier nominators," *Comput. Statist. Data Anal.*, vol. 34, no. 3, pp. 279–298, 2000.

[27] L. Gao, Q. Guo, A. Plaza, J. Li, and B. Zhang, "Probabilistic anomaly detector for remotely sensed hyperspectral data," *J. Appl. Remote Sens.*, vol. 8, no. 1, 2014, Art. no. 0 83538.

[28] Y. Zhang, Y. Fan, and M. Xu, "A background-purification-based framework for anomaly target detection in hyperspectral imagery," *IEEE Geosci. Remote Sens. Lett.*, vol. 17, no. 7, pp. 1238–1242, Jul. 2020.

[29] Z. Hou, W. Li, L. Gao, B. Zhang, P. Ma, and J. Sun, "A background refinement collaborative representation method with saliency weight for hyperspectral anomaly detection," in *Proc. IEEE Int. Geosci. Remote Sens. Symp.*, 2020, pp. 2412–2415.

[30] M. Dalla Mura, J. Benediktsson, B. Waske, and L. Bruzzone, "Morphological attribute profiles for the analysis of very high resolution images," *IEEE Trans. Geosci. Remote Sens.*, vol. 48, no. 10, pp. 3747–3762, Oct. 2010.

[31] M. Dalla Mura, J. Benediktsson, B. Waske, and L. Bruzzone, "Extended profiles with morphological attribute filters for the analysis of hyperspectral data," *Int. J. Remote Sens.*, vol. 31, no. 22, pp. 5975–5991, 2010.

[32] M. Dalla Mura, A. Villa, J. Benediktsson, J. Chanussot, and L. Bruzzone, "Classification of hyperspectral images by using extended morphological attribute profiles and independent component analysis," *IEEE Geosci. Remote Sens. Lett.*, vol. 8, no. 3, pp. 542–546, May 2011.

[33] X. Kang, X. Zhang, S. Li, K. Li, J. Li, and J. A. Benediktsson, "Hyperspectral anomaly detection with attribute and edge-preserving filters," *IEEE Trans. Geosci. Remote Sens.*, vol. 55, no. 10, pp. 5600–5611, Oct. 2017.

[34] J. Tropp and S. Wright, "Computational methods for sparse solution of linear inverse problems," *Proc. IEEE*, vol. 98, no. 6, pp. 948–958, Jun. 2010.

[35] J. Tropp and A. Gilbert, "Signal recovery from random measurements via orthogonal matching pursuit," *IEEE Trans. Inf. Theory*, vol. 53, no. 12, pp. 4655–4666, Dec. 2007.

[36] W. Dai and O. Milenkovic, "Subspace pursuit for compressive sensing signal reconstruction," *IEEE Trans. Inf. Theory*, vol. 55, no. 5, pp. 2230–2249, May 2009.

[37] A. Bruckstein, D. Donoho, and M. Elad, "From sparse solutions of systems of equations to sparse modeling of signals and images," *SIAM Rev.*, vol. 51, no. 1, pp. 34–81, 2009.

[38] X. Li and B. Zhao, "Video distillation," *Sci. China Inf. Sci.*, vol. 51, no. 5, pp. 685–764, 2021, doi: 10.1360/SSI-2020-0165.

[39] S. Chang, B. Du, and L. Zhang, "A sparse autoencoder based hyperspectral anomaly detection algorithm using residual of reconstruction error," in *Proc. IEEE Int. Geosci. Remote Sens. Symp.*, 2019, pp. 5488–5491.

[40] P. Salembier, A. Oliveras, and L. Garrido, "Antiextensive connected operators for image and sequence processing," *IEEE Trans. Image Process.*, vol. 8, no. 4, pp. 555–570, Apr. 1998.

[41] M. Farrell and R. Mersereau, "On the impact of PCA dimension reduction for hyperspectral detection of difficult targets," *IEEE Geosci. Remote Sens. Lett.*, vol. 2, no. 2, pp. 192–195, Apr. 2005.

[42] X. Li, M. Chen, F. Nie, and Q. Wang, "Locality adaptive discriminant analysis," in *Proc. 26th Int. Joint Conf. Artif. Intell.*, 2017, pp. 2201–2207.

[43] E. Breen and R. Jones, "Attribute openings, thinnings, and granulometries," *Comput. Vis. Image Understanding*, vol. 64, no. 3, pp. 377–389, 1996.

[44] S. Li, K. Zhang, P. Duan, and X. Kang, "Hyperspectral anomaly detection with Kernel isolation forest," *IEEE Trans. Geosci. Remote Sens.*, vol. 58, no. 1, pp. 319–329, Jan. 2020.

[45] J. Kerekes, "Receiver operating characteristic curve confidence intervals and regions," *IEEE Geosci. Remote Sens. Lett.*, vol. 5, no. 2, pp. 251–255, Apr. 2008.

Mingliang Xu received the B.E. and M.E. degrees from Zhengzhou University, Zhengzhou, China, in 2005 and 2008, respectively, and the Ph.D. degree from the State Key Laboratory of Computer-Aided Design and Computer Graphics, Zhejiang University, Hangzhou, China, in 2012, all in computer science.

He is currently an Associate Professor with the School of Information Engineering, Zhengzhou University. His research interests include computer graphics and computer vision.

Matjaž Perc received the Ph.D. degree from the University of Maribor, Maribor, Slovenia, in 2007.

He is currently a Professor of Physics and the Director of the Complexity Science Laboratory, University of Maribor. He is among top 1% most cited physicists according to Clarivate Analytics.

Dr. Perc is a member of Academia Europaea and the European Academy of Sciences and Arts. He is the 2015 recipient of the Young Scientist Award for Socio and Econophysics from the German Physical Society, and the 2017 USERN Laureate. In 2018, he received the Zois Award, which is the highest national research award in Slovenia. In 2019, he became a Fellow of the American Physical Society. He is an Editor for *Physics Letters A*, *Chaos*, and *Solitons & Fractals*. He is on the Editorial Board of *New Journal of Physics*, *Proceedings of the Royal Society A*, *Journal of Complex Networks*, *Europhysics Letters*, *European Physical Journal B*, *Scientific Reports*, *Royal Society Open Science*, *Applied Mathematics and Computation*, and *Frontiers in Physics*.

Ju Huang received the B.E. in measurement and control technology and M.E. in instrument science and technology degrees from the University of Electronic Science and Technology of China, Chengdu, China, in 2013 and 2016, respectively. He is currently working toward the Ph.D. degree with the University of Chinese Academy of Sciences, Beijing, China.

He is also an Assistant Research Fellow with the Xi'an Institute of Optics and Precision Mechanics, Chinese Academy of Sciences, Xi'an, China. His research interests include remote sensing, hyperspectral image processing, and machine learning.

Xuelong Li (Fellow, IEEE) is a Full Professor with the School of Artificial Intelligence, Optics, and Electronics, Northwestern Polytechnical University, Xi'an, China. He was the Founder of the Shaanxi Key Laboratory of Ocean Optics.

Kang Liu received the bachelor's degree in computer science and technology from Xi'an Jiaotong University, Xi'an, China, in 2013, and the master's degree in signal and information processing in 2016 from the University of Chinese Academy of Sciences, Beijing, China, where he is currently working toward the Ph.D. degree.

He is also an Assistant Research Fellow with the Xi'an Institute of Optics and Precision Mechanics, Chinese Academy of Sciences, Xi'an. His research interests include machine learning, computer vision, and remote sensing.